Atmospheric
Measurement
Techniques

Seasonal and intra-diurnal variability of small-scale gravity waves in OH airglow at two Alpine stations

Patrick Hannawald[1], Carsten Schmidt[2], René Sedlak[1], Sabine Wüst[2], and Michael Bittner[1,2]

[1]University of Augsburg, Institute of Physics, Augsburg, Germany
[2]German Aerospace Center, German Remote Sensing Data Center, Oberpfaffenhofen, Germany

Correspondence: Patrick Hannawald (patrick.hannawald@physik.uni-augsburg.de)

Abstract. Between December 2013 and August 2017 the instrument FAIM (Fast Airglow IMager) observed the OH airglow emission at two Alpine stations. A year of measurements was performed at Oberpfaffenhofen, Germany (48.09° N, 11.28° E) and 2 years at Sonnblick, Austria (47.05° N, 12.96° E). Both stations are part of the network for the detection of mesospheric change (NDMC). The temporal resolution is two frames per second and the field-of-view is 55 km × 60 km and 75 km × 90 km at the OH layer altitude of 87 km with a spatial resolution of 200 and 280 m per pixel, respectively. This resulted in two dense data sets allowing precise derivation of horizontal gravity wave parameters. The analysis is based on a two-dimensional fast Fourier transform with fully automatic peak extraction. By combining the information of consecutive images, time-dependent parameters such as the horizontal phase speed are extracted. The instrument is mainly sensitive to high-frequency small- and medium-scale gravity waves. A clear seasonal dependency concerning the meridional propagation direction is found for these waves in summer in the direction to the summer pole. The zonal direction of propagation is eastwards in summer and westwards in winter. Investigations of the data set revealed an intra-diurnal variability, which may be related to tides. The observed horizontal phase speed and the number of wave events per observation hour are higher in summer than in winter.

1 Introduction

Hydroxyl (OH) airglow, originally investigated by Meinel (1950), can be used as a tracer for atmospheric dynamics in the middle atmosphere, especially for the investigation of gravity waves (Peterson, 1979; Taylor et al., 1993; Gardner and Taylor, 1998 and many more). The OH airglow layer is located at about 87 km altitude and has a half-width (full width at half maximum) of roughly 8 km (Baker and Stair Jr., 1988). Newer studies, for example from von Savigny (2015) or Wüst et al. (2017), show that the altitude change can be up to a few kilometres, also the shape of the distribution with height may vary. Many OH bands contribute to the overall intensity in the visible and short-wave infrared range (see e.g. Rousselot et al., 2000). However, the intensity in the short-wave infrared is much higher than in the visible range. Therefore, exposure times of instruments observing the OH airglow can be much lower when addressing the short-wave infrared emissions (mainly OH(3-1) and OH(4-2)). Thus, the temporal resolution of the FAIM data is comparatively high, up to two frames per second (Hannawald et al., 2016; Sedlak et al., 2016).

Changes in pressure and temperature lead to intensity fluctuations in the OH layer. These perturbations can be measured and are most often caused by atmospheric gravity waves or other atmospheric wave types. Gravity wave parameters such as horizontal wavelength and observed phase speed can be derived from images of the OH airglow layer (see Peterson, 1979; Taylor et al., 1995; Hecht et al., 2000; Nakamura et al., 1999; Mukherjee et al., 2010; Pautet et al., 2014 and others).

It is well known that gravity waves influence circulation on a global scale (see Fritts and Alexander, 2003 for an overview). The residual meridional circulation in the meso-sphere is driven by breaking gravity waves (Holton, 1983; Baker, 2009). In this context small-scale and short-period gravity waves are of particular interest (Fritts and Vincent, 1987).

Gravity waves are often generated in the troposphere, when large horizontal flows of air masses encounter obstacles and get displaced vertically. Mountain ridges or coast-lines can serve as such an obstacle. In Europe, the Alps sig-nificantly influence large scale flows in the troposphere. De-pendent on the vertical wind structure, some of these waves can travel upward up to the mesosphere. In order to in-vestigate the characteristics of gravity waves, a short-wave infrared imager has been deployed at two Alpine stations (belonging to the network for the detection of mesospheric change; https://ndmc.dlr.de, last access: 10 January 2019) that observed the OH airglow with high spatio-temporal res-olution for over 3 years. This gives a rather large and dense data set of OH airglow images which is investigated for the first time in this study. The focus of the investigation is on small-scale gravity waves with horizontal wavelengths smaller than 50 km.

In Sect. 2, the instrument, the data basis, and data prepro-cessing is briefly described. Section 3 explains the analysis in detail, including the derivation of the unambiguous prop-agation direction, phase speed, and period of the waves. The results are presented in Sect. 4 and discussed in Sect. 5.

2 Instrumentation and data

The instrument FAIM 1 (Fast Airglow IMager) is based on a cooled InGaAs-photodiode array (256 pixel × 320 pixel) with a spectral sensitivity from about 0.9 to 1.65 µm. Due to the spectral intensity distribution of the OH airglow emission (e.g. Rousselot et al., 2000) the emissions of mainly OH(3-1) and OH(4-2) contribute to the observed intensity (see e.g. Hannawald et al., 2016 for further information). Therefore, the possible acquisition time for the images is comparatively low allowing for a temporal resolution of two frames per sec-ond. Equipped with a narrow angle lens with a field-of-view (FOV) of 19.5 to 24.1°, the spatial resolution is compara-tively high. The observed area at 87 km is large enough to in-vestigate both small-scale gravity waves (up to about 50 km horizontal wavelength) as well as instability structures (down to horizontal scales of 200 m). Further details concerning the instrument, its FOV, spatial resolution, and comparison to spectrometer data are given in Hannawald et al. (2016).

From 17 December 2013 to 26 January 2015, FAIM 1 was located at Oberpfaffenhofen (OPN), Germany (48.09° N, 11.28° E) with a zenith angle of 45°. The resulting average resolution at the height of the OH airglow layer is about 200 m pixel^{-1} and the covered area is 55 km × 60 km. The
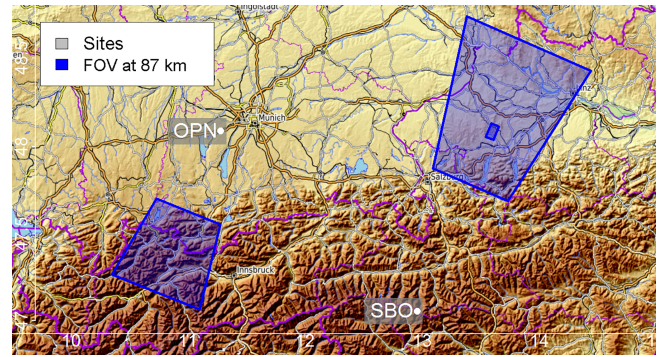
Figure 1. The two instrument sites in the Alpine region, Oberp-faffenhofen (OPN, 2013–2015) and Sonnblick Observatory (SBO, 2015–2017). Observed areas at 87 km altitude from OPN (left trapezium) and SBO (right trapezium) are drawn in blue. Both sta-tions belong to the NDMC.

average resolution is calculated by $\sqrt{\frac{A}{N}}$ with the area of the trapezium A and the number of pixels N. The resolution of the x axis r_x (along the top and base side of the trapez-ium, respectively) ranges from 142 to 199 m pixel^{-1}. For the y axis along the zenith angle, the resolution r_y ranges from 174 to 348 m pixel^{-1} calculated by $r_y = h \cdot (\arctan(\phi_2) - \arctan(\phi_1))$, with the airglow layer height h of 87 km and ϕ_2 and ϕ_1 the elevation angles of two subsequent pixels. The effective pixel size $\left(\sqrt{r_x \cdot r_y}\right)$ therefore ranges from 157 to 263 m pixel^{-1}. Also, see Fig. 3 in Hannawald et al. (2016) for the change of average resolution when tilting the instru-ment along the zenith angle.

From 3 August 2015 to 26 July 2017, the instrument was located at Sonnblick Observatory (SBO), Austria (47.05° N, 12.95° E). The zenith angle of 55° for the second configu-ration is higher and corresponds to a larger observed area and a smaller average spatial resolution (70 km × 95 km and 280 m pixel^{-1}, respectively). The x axis resolution ranges from 164 to 269 m pixel^{-1} and the y axis resolution ranges from 234 to 636 m pixel^{-1}, therefore the effective pixel sizes are 195 to 413 m pixel^{-1}.

The position and size of the FOV within the Alps and at their foothills can be read from Fig. 1, where the left FOV corresponds to the site OPN and the right FOV to SBO. The OPN data are acquired above the mountains whereas the SBO data are acquired from the northern Alpine foothills.

For the whole observation period the integration time of the camera was set to 0.5 s. For several nights in the first quarter of 2014, a long pass filter was used to limit the spec-tral sensitivity to 1.3–1.65 µm to exclude contributions from $O_2(0-0)$ at 1.27 µm. In our later study (Hannawald et al., 2016), we showed that the contribution of O_2 to the recorded signal is negligible. So, the filter is not required and was therefore removed during later observations. However, these modifications do not influence the desired wave parameters. For SBO the settings stayed unchanged for the whole time

period. It should be noted that the entire analysis focusses on the intensity distribution within each image and not on seasonal or day-to-day changes of airglow intensity.

The number of acquired images per month is depicted in Fig. 2. The black bars show the images with clear sky conditions which are used for analysis. The stacked grey bars correspond to images not analysed due to cloud cover or moonlight visible in the FOV. The periods with good weather conditions were carefully selected by manually checking keograms and, where necessary, inspecting the image sequences of the respective time frames by eye.

For both stations each month is represented by more than a 100 000 images (Fig. 2). The maximum number of images in 1 month is almost 2 million in December 2016. The 7.2 million images (about 1000 h of airglow observation) of data for OPN are analysed as well as 14.8 million images (about 2000 h) for SBO. Overall, 28 % of all data are found to be good and are analysed.

The preprocessing of the images is explained in the following paragraphs. First, the images are flat fielded to correct them for fixed pattern noise and camera artefacts. This includes removing dead pixels with interpolation over neighbouring pixels. Figure 3 shows the steps of preprocessing for an exemplary image where (a) corresponds to the flat fielded image. Additionally, a Gaussian blur is applied to the image with a kernel size of three to reduce high frequency noise. The kernel (a 3×3 matrix) is calculated with $k(x, y) = \frac{1}{2\pi\sigma^2} \cdot \exp\left(-\frac{x^2+y^2}{2\sigma^2}\right)$; $x, y \in (-1, 1)$ with $\sigma = 1$ and then normalised, so that the sum of all matrix values equals 1. The pixels of the smoothed image ($I_{\text{smoothed}}(x, y)$) are calculated as follows, which is commonly called convolution of an image I with a kernel k (Kaehler and Bradski, 2017):

$$I_{\text{smoothed}}(x, y) = \sum_{i=-1}^{1} \sum_{j=-1}^{1} I(x+i, y+j) \cdot k(i, j). \tag{1}$$

Figure 3b shows the result of the star removal. Due to the high spatial resolution, stars usually cover several pixels (in individual cases up to 50 pixels/star) and are present in every image showing airglow. Therefore, an optimal star removal requires a sophisticated approach, otherwise too many pixels will be modified. The star removal algorithm consists of three steps.

1. Identification of stars based on a threshold value: first a median blur is applied to image (a). The blurred image is subtracted from image (a). The stars remain as the high frequency parts of the image. All pixels with values above a pre-defined start threshold are considered to be stars. This normally identifies more than one but not all pixels influenced by the star, so further characterisation is needed.

2. The characterisation of each star is performed by finding its centre (denoted as star seed) and radius in order to get all pixels influenced by the star (denoted as star pixels): the maximum value of each star is searched and taken as the centre of the star. The radius of the star is determined by looking at the four main directions from the star seed (top, bottom, left, right). Starting at the star seed, the distance in each direction is increased individually for as long as the intensity value is lower than the former value in the respective direction. The maximum distance of the directions is taken as the star radius. All pixels in a circle around the star seed within the star radius are considered as star pixels.

3. All star pixels are interpolated by its nearest (non-star pixel) neighbours.

To overcome the arbitrary threshold in step 1, steps 1 and 2 are repeatedly applied on the original image with a slightly increased or decreased threshold for each iteration. This is done for as long as the number of overall star pixels is between 2 % and 7 % of all pixels. The final threshold is then used for the actual star removal.

The starless image (Fig. 3b) is then unwarped to an equidistant grid resulting in a trapezium shaped FOV. The unwarping depends on the zenith angle of 55° (45° for OPN) following the procedure described in Hannawald et al. (2016). Furthermore, the image is flipped around the vertical axis to get a satellite's view, which can be projected onto a map (east is on the right side of the image). Figure 3c shows the result of this step. The largest possible square-shaped area within the trapezium is taken from the unwarped image (c) in order to prevent directional differences due to the shape of the analysed area. The result is shown in Fig. 3d.

Both mean intensity and linear trend (i.e. a plane calculated by a two-dimensional linear regression) are subtracted from Fig. 3d. The image is then multiplied with a Kaiser–Bessel window (alpha = 4, Kaiser and Schafer, 1980) so that the edges fade to zero. The Kaiser–Bessel window has been chosen for its high side-lobe damping. Additionally, zero-padding is applied to further improve and resolve the peaks of the following Fourier analysis more clearly.

3 Analysis

Due to the huge amount of data, an automatic approach is necessary for the analysis. The two-dimensional fast Fourier transform (2D-FFT, or even 3D-FFT) is often used to extract wave parameters from airglow images (e.g. Gardner et al., 1996; Garcia et al., 1997; Coble et al., 1998; Matsuda et al., 2014 and others). The focus of this article is on the automatic analysis of the Fourier spectra, i.e. on identifying peaks, combining the information of consecutive images, grouping the results in wave events, and investigating them individually.

The previously described preprocessing steps are performed for each image and the FFT is calculated sub-
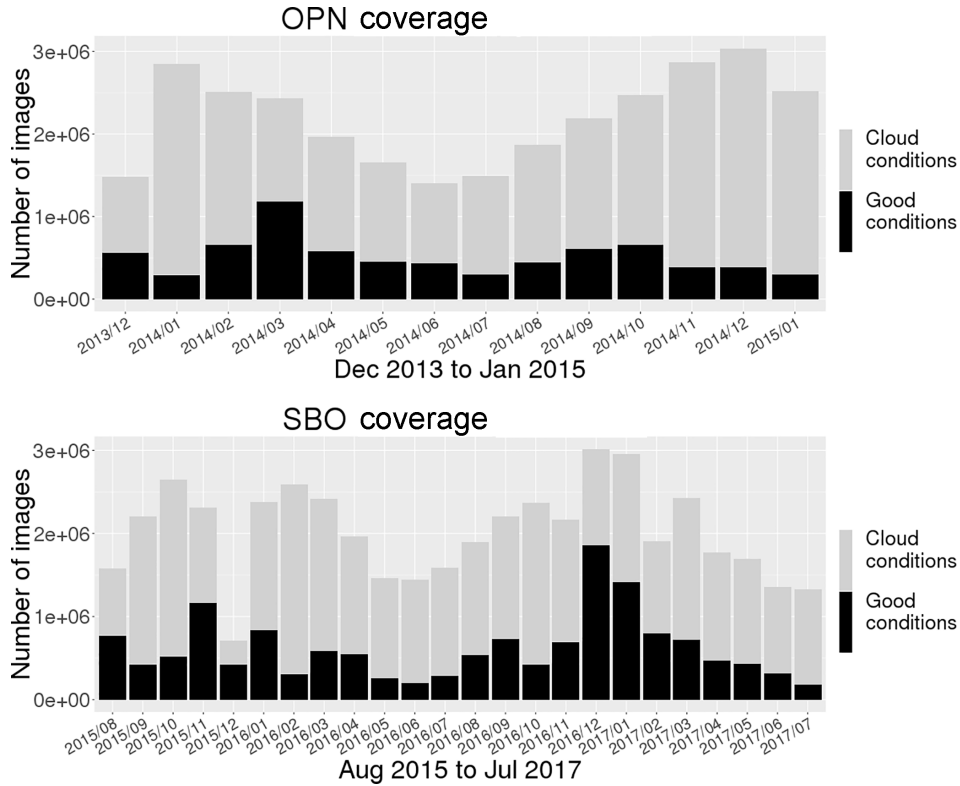
Figure 2. Overview of the data sets for both stations Oberpfaffenhofen (OPN) and Sonnblick Observatory (SBO). The coverage is grouped by month. The black bars show the number of images with good observation conditions which are used for analysis. The grey bars give the portion of images with bad conditions, e.g. cloud cover or intense moonlight.

sequently. The resulting two-dimensional complex spectra are then analysed for the major peaks. Figure 3e shows the Fourier magnitude spectrum ($\text{Mag} = \sqrt{Re^2 + Im^2}$). The point of origin of k_x and k_y is at the centre of the spectrum. In Fig. 3e just the middle part of the spectrum is shown as the rest is not significant.

In order to identify the peaks in the Fourier spectrum a significance level is estimated. Accordingly, for each preprocessed image 100 random matrices based on the standard deviation of the preprocessed image are created and the 2D-FFT is applied to them in the same manner. For each of the 100 random spectra the magnitude is calculated and the respective maximum values are extracted. The 95 % percentile of these maxima is then taken as significance level. Values lower than the significance level (red contour in Fig. 3e) are excluded from further analysis.

Now the peaks in the spectrum have to be identified and distinguished correctly. Therefore, a local maximum search is accomplished: a sliding window of 5×5 pixels is shifted over the spectrum. If none of the neighbouring pixels are higher than the pixel in the centre of the window, then this pixel is treated as a local maximum. For all local maxima at position (x', y') the amplitude A is determined by

$$A = \sqrt{Re(x', y')^2 + Im(x', y')^2}. \qquad (2)$$

The FFT reconstructs the image by superposing plane waves. If a wave signal is not adequately described by a plane wave (e.g. the wave crests and valleys are curved or show other irregularities) it will be composed of additional plane wave components. This leads to the fact that in some cases more than 10 different wave components are found in one image. Before further simplifying these cases, all signals are kept if they have at least 10 % of the intensity of the signal with the highest amplitude.

For visualization purposes Fig. 3f shows the reconstruction of the original image based on the four (point-symmetric) local maxima identified in the spectrum and their derived parameters (marked as blue dots in Fig. 3e). Panel (g) shows the four individual wave signatures as plane waves separately.

For each of these maxima, the wave parameters horizontal wavelength λ, angle of propagation α, and phase φ are determined as follows:

$$\lambda = \frac{1}{\sqrt{k_x^2 + k_y^2}}, \qquad (3)$$

$$\alpha = \arctan\left(\frac{k_y}{k_x}\right), \qquad (4)$$

and
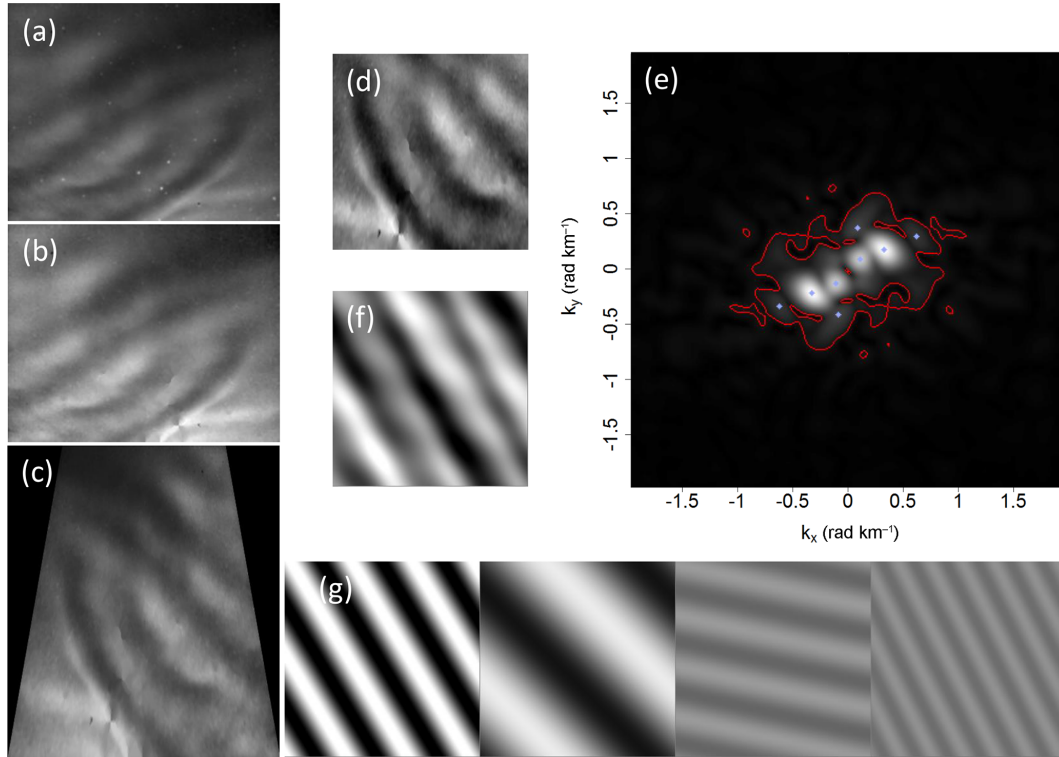
Figure 3. Preprocessing steps explained for one image 26 May 2016 01:52:41 UTC. For display reasons the contrast is adjusted for each image. **(a)** Flat-fielded image with Gaussian blur (kernel size 3) applied, **(b)** result of star removal, **(c)** image unwarped to equidistant grid and flipped around y axis for satellite's view, **(d)** image cropped to square size, **(e)** middle section of point-symmetric FFT magnitude spectrum (red line: significant level, blue dots: identified maxima), **(f)** superposition of the four reconstructed plane waves, and **(g)** the four plain waves side by side.

$$\varphi = \arctan\left(\frac{Im(x', y')}{Re(x', y')}\right). \tag{5}$$

In order to bring together the signals extracted from each image individually, the wave signatures (waves with identical wavelength and identical angle of propagation) are grouped into so-called wave events. It is assumed that a wave (band) or an instability feature with a wave-like appearance (ripple) will last for more than just a few seconds and should therefore be detected in several consecutive images, possibly with gaps of a few images. These groups of identical signatures in a given time interval are henceforth denoted as wave events. A new signature is attributed to a previously identified wave event if it occurs within less than 30 s after the last known signature of the (known) wave event.

Each wave event with more than two occurrences of the respective wave signature (wave signature found in more than two images) is analysed in order to derive the overall time of occurrence, phase speed, period, and unambiguous direction of propagation. Through linear regression the mean phase shift with time is determined from the phase information contained in the FFT. Phase jumps are considered in order to get the correct slope of the linear regression. The reciprocal absolute value of the slope gives the period T of the wave event.

With the phase shift with time $\dot{\varphi} = \frac{\Delta\varphi}{\Delta t}$ and the horizontal wavelength the horizontal phase speed v can be calculated as follows:

$$v = \lambda \cdot |\dot{\varphi}|. \tag{6}$$

The sign of $\dot{\varphi}$ also provides the unambiguous direction of propagation.

Further statistical values are determined for each wave event such as the length of the time interval, in which the respective wave is observed, referred to as presence time of the event, and the number of occurrences within the presence time, which is an important indicator for the persistence of the wave event. These parameters are used as indicators to decide whether an event can be considered as an "important" wave. To be considered any further, an event has to be present for at least 2 min (240 images) in which the respective wave signature has to be found at least 100 times. The derived horizontal phase speed should be larger than $3 \, \mathrm{m \, s^{-1}}$ and the residual standard error of the linear regression less than $7°$. These values were empirically derived from extensive testing.

Through this kind of filtering, very small-scale waves or instability features (smaller than 5 to 10 km horizontal wavelength) are under-represented as these signals change rapidly

and are present for only a small amount of time. This has to be considered when interpreting the results. In this study, we focus on the more persistent wave events. Regarding the FOV, the side length of the analysed regions is 47 km for OPN and 61 km for SBO. FFT results with larger horizontal wavelengths (e.g. due to the wave being arranged along the diagonal line of the analysed region) are excluded from further interpretation.

4   Results

For investigating the results, the data sets are split into the summer (April to September) and winter (October to March) seasons. The predominant propagation direction in summer is similar for both stations (OPN and SBO) and is towards the north-east (NE) direction (Fig. 4). More than 46 % (OPN) and 55 % (SBO) of the waves propagate in this direction. During winter, the main propagation direction derived from OPN data is south-west (NE: 15 %, SE: 21 %, SW: 38 %, NW: 26 %). At SBO, the main propagation direction during winter is north-west and south-west (NE: 16 %, SE: 22 %, SW: 27 %, NW: 36 %).

Integrated over summer and winter, about 48 % (OPN) and 26 % (SBO) of the waves have less than 15 km horizontal wavelength. As mentioned above, the data filtering process underestimates small-scale waves (Fig. 4). Therefore, these small-scale waves are obviously quite persistent. Medium-scale waves with wavelengths from 15 km to two thirds of the respective FOV represent 34 % (OPN) and 55 % (SBO) of the detected waves. Larger-scale waves up to the side length of the FOV represent about 20 % of all waves.

For OPN, the amount of small-scale waves tends to be larger in winter with 51 % in comparison to 45 % in summer (within the above mentioned uncertainties caused due to the filter process). For medium- and large-scale waves (wavelengths larger than 15 km) the situation reverses (49 % during winter and 55 % during summer), however, this seasonal difference is quite low. At SBO, the situation is qualitatively similar. The occurrence rate is about 31 % during winter and 21 % during summer for the small-scale waves and 70 % during winter and 79 % during summer for the medium- and large-scale waves.

The number of wave events normalised to the amount of available airglow observation-hours by season at OPN shows a density of 6.1 events per hour during summer and 3.6 events per hour during winter. At SBO, the density is 7.1 events per hour in summer and 4.2 events per hour in winter. Thus, the density in winter is only 60 % as high as in summer.

In order to investigate the intra-diurnal variation of the direction of propagation, all wave events are binned according to the time of day of their occurrence (Fig. 5). The directions are grouped into the four quadrants NE, SE, SW, NW. Panels (a), (b), (e), and (f) show the distribution of wave events with time. Mainly due to the variation of the length of night,

the maximum of wave events is around midnight (approx. 22:00 to 01:00 UTC). The relative distribution of the different directions (Fig. 5c, d, g, h) reveals considerable intra-diurnal variations. Obviously, the propagation towards the north-east (NE) direction (red) is dominant with more than circa 40 % of the wave events for almost all hours (Fig. 5c and d). In winter, the SW direction (green) is prevalent at OPN and the NW and SW direction (blue and green) at SBO (Fig. 5g and h), as already seen from Fig. 4. In general, there is a notable anti-correlation for opposing directions (NE to SW and NW to SE). However, the correlation coefficients underlie high uncertainties due to only few available data points and – more importantly – an unequal distribution of wave events which leads to an overestimation of the early and late night hours. The propagation direction towards NE at SBO summer (Fig. 5d), shows an oscillation-like pattern with a maximum at 23:00 UTC. A shorter period oscillation may be seen at SBO winter NE direction (Fig. 5h) with a maximum at 01:00 UTC and a minimum at 21:00 UTC. However, the derivation of specific periods is impossible here, because the length of the night is of the order of the periods.

The distributions of observed horizontal phase speeds are shown in Figs. 6 and 7. Figure 6 depicts the absolute values. During OPN winter, the maximum of the distribution is around $9\,\mathrm{m\,s^{-1}}$ with a secondary peak at about $25\,\mathrm{m\,s^{-1}}$. For OPN summer, the distribution is not as smooth as during winter (with peaks at about 5, 10, 18, 23, 30, 38, and $42\,\mathrm{m\,s^{-1}}$). The SBO distributions reveal peaks at 7 and $13\,\mathrm{m\,s^{-1}}$ in winter and 23 and $35\,\mathrm{m\,s^{-1}}$ in summer. The 95 % quantile of phase speed is 46 and $52\,\mathrm{m\,s^{-1}}$ considering both seasons and all directions, thus just a few of the observed wave events propagate faster than that.

Table 1 shows the mean values and standard deviation of the phase speeds as a function of the direction. For both stations, the mean values are higher during summer than during winter with an increase of about 7 % (OPN, 22.2 to $20.7\,\mathrm{m\,s^{-1}}$) and 9 % (SBO, 25.5 to $23.5\,\mathrm{m\,s^{-1}}$). The observed horizontal phase speeds in the SW direction during summer and NW direction during winter are significantly lower compared to the other directions (Table 1). Especially in summer, the phase speeds are higher in eastward direction (NE and SE together) than in westward direction (SW and NW together). During winter at SBO it is similar, but for OPN winter, the behaviour is different (NE lower phase speed than SW).

Figure 7 shows the distributions separated into zonal and meridional phase speeds. The dashed lines give the mean values of the distributions. For zonal and meridional phase speeds, respectively, and for both stations, the mean values are higher in summer than in winter. The mean values of all SBO distributions are higher (more toward positive numbers) than the respective equivalents of OPN distributions. Table 2 gives additional information about the distributions. These are approximately symmetric with skewness values smaller than 0.37 except for the zonal directions in winter where the distributions are right-skewed with values 0.61 and 0.95 (the
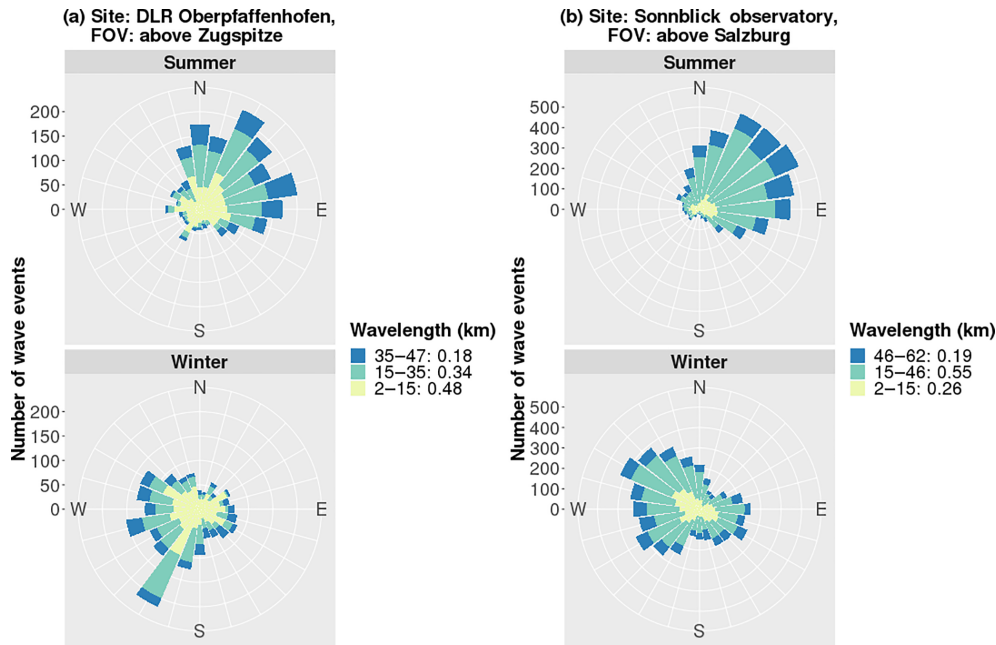
Figure 4. Directions of gravity wave propagation at Oberpfaffenhofen (**a**, 48.09° N, 11.28° E) and Sonnblick (**b**, 47.05° N, 12.95° E). The top (bottom) panels show the data for the summer (winter) season. The colours refer to the horizontal wavelengths and are separated into small-scale waves (< 15 km), medium-scale waves (≥ 2/3 of the FOV: 35 and 46 km, respectively) and larger-scale waves (up to the side length of the respective FOV; 47 and 62 km, respectively). The numbers next to the wavelength legend represent the proportion of the respective bin.

Table 1. Mean (standard deviation) values of absolute horizontal phase speed as a function of the station, season, and direction.

Station	Season	NE	SE	SW	NW	All
OPN	Summer	24.4 (13.1)	22.6 (14.2)	17.4 (12.4)	19.9 (14.1)	22.2 (13.7)
OPN	Winter	19.6 (13.5)	23.9 (17.3)	22.0 (12.4)	17.0 (10.7)	20.7 (13.6)
SBO	Summer	26.3 (13.5)	25.0 (15.6)	17.9 (13.4)	26.3 (14.6)	25.5 (14.3)
SBO	Winter	27.5 (17.5)	27.7 (20.7)	22.1 (13.5)	20.2 (12.1)	23.5 (15.9)

standard error of the skewness, defined as $\sqrt{\frac{6}{N}}$ (Press et al., 2007) where N is the number of wave events, is 0.04 (OPN) and 0.02 (SBO)). The standard deviation at SBO is higher than for OPN. For the zonal direction in winter this difference is highest with 28 % increase (20.9 (SBO) to 16.3 (OPN)).

The observed wave periods are shown in Fig. 8. The 10 % and 90 % quantiles of the distribution of periods range from about 6 to 50 min (OPN) and from 7 to 70 min (SBO). More than 60 % of the wave events have periods between 10 and 60 min. Around 20 % of the waves show periods close to the Brunt–Väisälä period with 5 up to 10 min. Note, that several events have periods smaller than 5 min, but extensive investigation of these events is beyond the scope of this study. The distributions of periods have maxima at about 8 and 10 min at OPN for summer and winter, respectively. At SBO, the maxima are at 13 and 7 min. The distributions are highly right-skewed with values 3.3 and 3.1 at OPN in summer and winter, and values of 3.3 and 2.8 at SBO.

The main results are summarised in the following list:

- The main zonal propagation direction is eastwards during summer and westwards during winter. The main meridional propagation direction is northwards during summer. During winter, the meridional propagation direction is southwards at OPN and northwards as well as southwards at SBO (Fig. 4).

- We found an intra-diurnal variability of the propagation directions. The opposing directions seem to be anti-correlated (NE to SW and NW to SE). Oscillations seem to be present in the data, but cannot be precisely determined (Fig. 5).

- The number of wave events per observation-hour, the means of zonal and meridional phase speeds, and the means of absolute horizontal phase speeds are higher in summer than in winter (Figs. 6, 7, and 8).
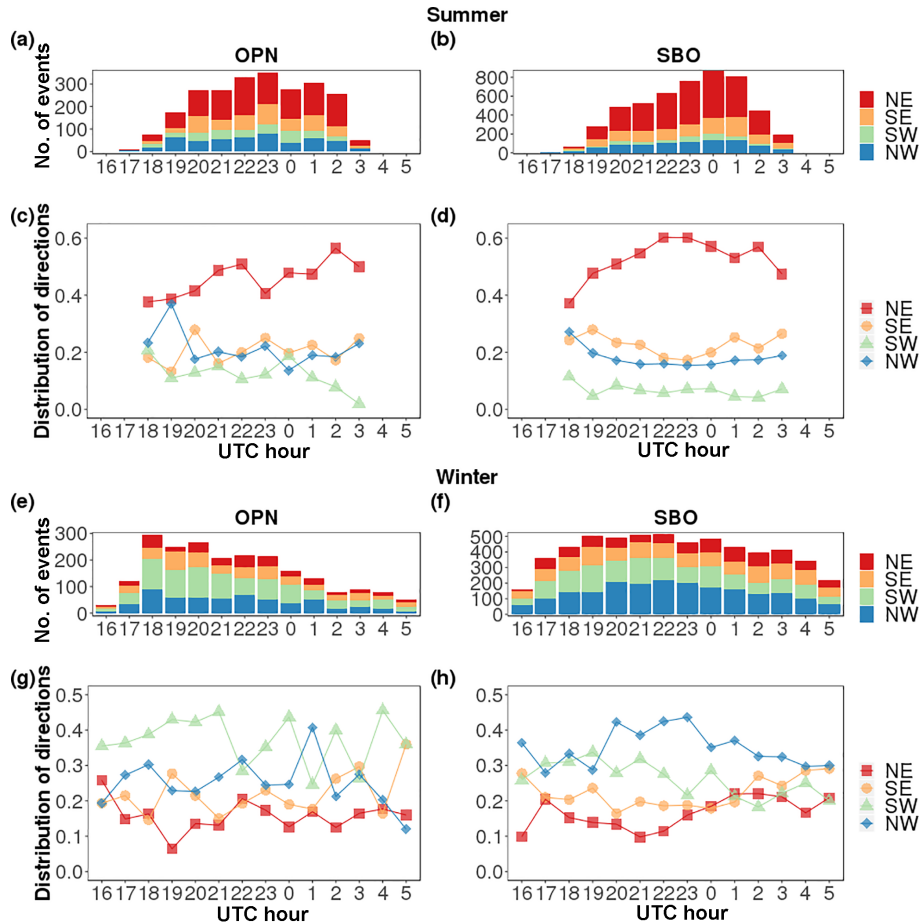
Figure 5. Number of gravity wave events and distribution of propagation directions as a function of time for OPN **(a, c, e, g)** and SBO (b, d, f, h). The top panels **(a)–(d)** refer to the summer season and the bottom panels **(e)–(h)** to the winter season. The data are grouped into north-east (NE), south-east (SE), south-west (SW) and north-west (NW) quadrants.
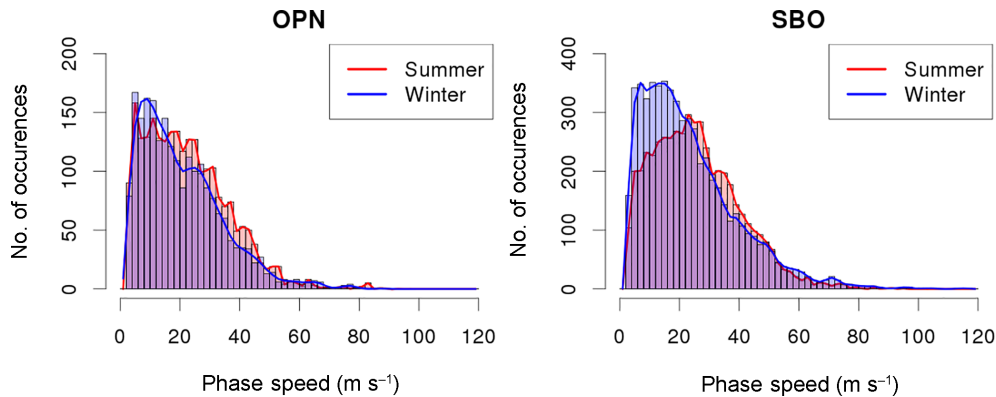

Figure 6. Absolute values of horizontal phase speed of the gravity wave events for OPN and SBO for the summer and winter seasons in $\mathrm{m\,s^{-1}}$.

5 Discussion

In order to understand the results it is essential to know which part of the gravity wave spectrum is actually observed by our instruments. The most important constraints on the observations are the OH layer thickness and the FOV of the instruments. The former is for example discussed in Gardner and Taylor (1998) who argue that the observed verti-
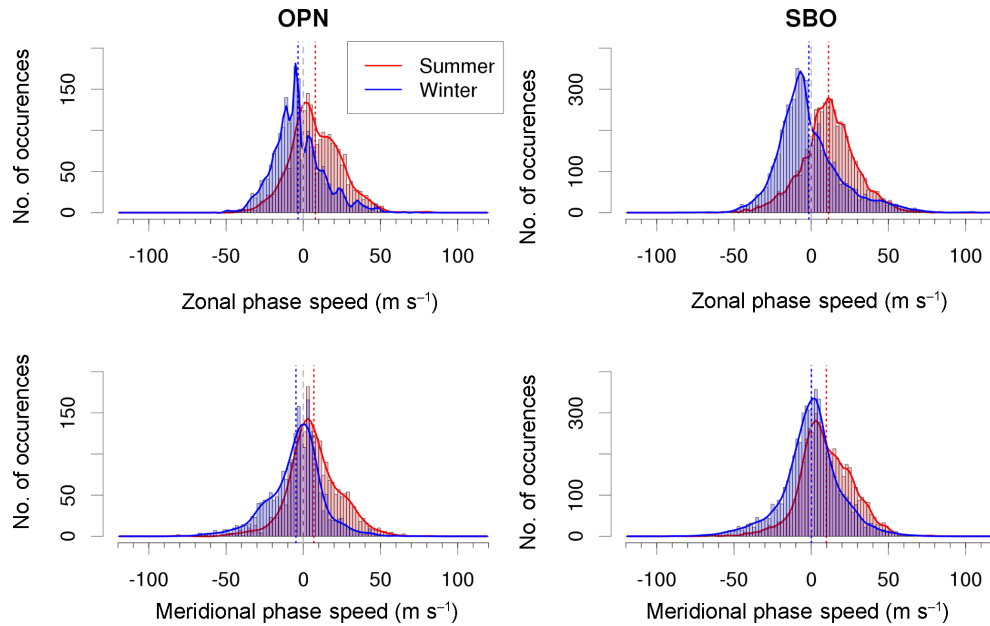
Figure 7. Horizontal phase speed of the gravity waves at OPN and SBO for summer and winter season in m s^{-1} separated by zonal and meridional components. Negative phase speed indicates westward or southward direction, and positive phase speed eastward or northward direction. The dashed grey line marks zero phase speed and the red and blue dotted lines refer to the mean values over the respective summer and winter distribution, respectively.

Table 2. Statistical moments of horizontal phase speed distributions for station, season, and direction. Negative phase speed indicates westward or southward direction, positive phase speed eastward or northward direction. The units of mean, median, standard deviation, and peak are m s^{-1}, the skewness is unitless. The positions of the peaks are determined on basis of the splines overlying the histograms in Fig. 7.

| Station	Season	Direction	Mean	Median	SD	Skewness	Peak
OPN	Summer	Zonal	7.8	6.2	16.6	0.32	1
OPN	Summer	Meridional	6.9	5.1	17.2	0.01	3
OPN	Winter	Zonal	−3.4	−4.9	16.3	0.61	−5
OPN	Winter	Meridional	−4.7	−2.8	17.7	−0.37	1
SBO	Summer	Zonal	11.2	11.4	18.0	−0.09	11
SBO	Summer	Meridional	9.8	8.3	17.6	−0.03	3
SBO	Winter	Zonal	−1.5	−5.1	20.9	0.95	−7
SBO	Winter	Meridional	0.1	0.8	19.1	−0.24	1

cal wavelengths have to be larger than the OH layer width. Wüst et al. (2016) showed in their Fig. 9c the reduction of the observed amplitude of a wave depending on the vertical wavelength for different values of the OH layer thickness. The horizontal wavelength is limited by the FOV (OPN: 47 km, SBO: 61 km). Figure 8 indicates that most periods are smaller than 1 h. Therefore, the waves contained in the data set are referred to small horizontal wavelength, high-frequency gravity waves which are known to be important for momentum transport (see Zhang et al., 2014) and which are of major importance for the mesospheric circulation (Garcia and Solomon, 1985; Fritts and Vincent, 1987).

The propagation directions of the gravity waves show a clear pattern of seasonal dependency. This behaviour for mesospheric gravity waves is not limited to the two Alpine stations OPN and SBO, but it is well known. For example Tang et al. (2014) and Vargas et al. (2015) compared several airglow observations of many research groups around the globe and find a meridional propagation towards the summer pole for many stations. The zonal component of the eastward propagation during summer and westward propagation during winter is also dominant at many stations.

The seasonal variation of the zonal propagation direction can be explained by zonal stratospheric wind fields when assuming that the observed waves originate from lower atmospheric layers or are directly influenced by waves from lower layers, for example by wave–wave interactions. There is a strong westward wind in summer and eastward wind in win-
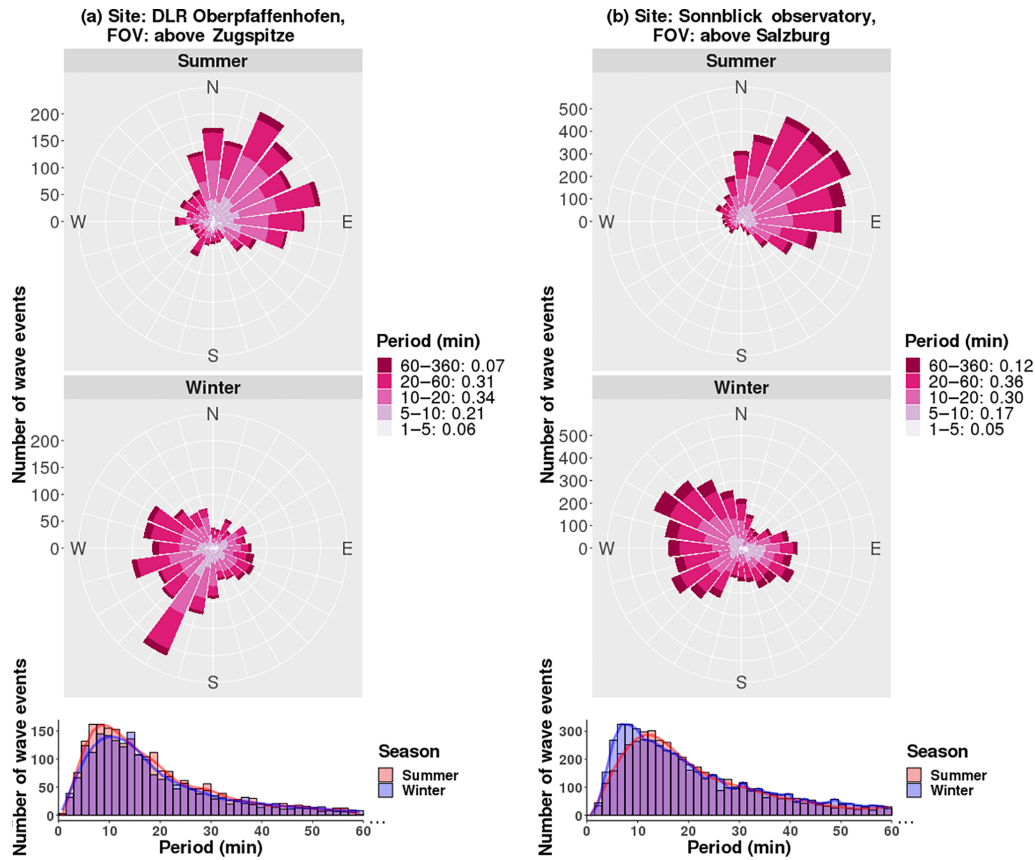
Figure 8. Top: the same as Fig. 4, but for the observed wave periods. Bottom: histograms of observed wave period for summer and winter season.

ter in the stratosphere (Fleming et al., 1990) filtering gravity waves which propagate with a lower speed in the same zonal direction. Thus, mostly eastward propagating gravity waves will be observed in summer and westward propagating gravity waves in winter. This is also confirmed for example by Taylor et al. (1993) and McLandress (1998).

In winter, waves with positive zonal phase speed should consequently be generated in situ or above the stratospheric jet (e.g. by wind shear), propagate from above down to the airglow layer, or pass the stratospheric jet when it is unusually weak. The stratospheric wind filtering could also explain the skewness of the zonal phase speed distributions, because the filtering is mainly affecting the slower eastward propagating waves in winter which are less likely to be observed in the mesosphere. Therefore, there is a bump in the distribution at these phase speeds.

The seasonal variation of the meridional propagation direction (Fig. 4) for summer season towards the north, for winter towards the south at OPN and towards the south and the north at SBO could be due to the meridional circulation in the mesosphere. According to Yuan et al. (2008) showing Na lidar data and global circulation model runs, the meridional circulation reverses in summer and winter (in summer: to the

south, in winter: to the north); additionally, it is much weaker in winter than in summer (about 10 to $14 \, \mathrm{m \, s^{-1}}$ southwards in summer and 0 to $6 \, \mathrm{m \, s^{-1}}$ northwards in winter strongly depending on the model and the parameters used; the lidar data at $41°$ N, $105°$ W with tides removed show higher values of up to $18 \, \mathrm{m \, s^{-1}}$ in summer and up to $14 \, \mathrm{m \, s^{-1}}$ in winter). Therefore, the filtering effect can be regarded as being stronger during summer than during winter. This could be an indication of the southward propagating summer waves to be more influenced and filtered out by the stronger meridional circulation while the winter waves are less influenced by the weaker meridional circulation and do not suffer such a strong filtering effect. This would explain the clear pattern during summer and the more arbitrary meridional propagation during winter, especially at SBO. However, there are alternative hypotheses concerning the seasonal dependency of meridional wave propagation. Vargas et al. (2015) lay out that neither the meridional circulation, which is too weak from their point of view, nor tides can explain this seasonal behaviour on a global scale. They suggest an interaction of the seasonally dependent (and strong) zonal wind with the lower thermosphere duct as described by Walterscheid et al. (1999).

At Oberpfaffenhofen, horizontal wavelengths and phase speeds were already derived in 2011 and 2015 (Wachter et al., 2015: February to July 2011; Wüst et al., 2018: July to November 2015; our data were acquired at SBO during the second time period). In these cases, a combination of three spectrometers and one scanning spectrometer, respectively, were used instead of an imaging system. The spectrometers are sensitive to larger horizontal wavelengths, which are related to a higher possible maximum of intrinsic phase speed (compare e.g. Fritts and Alexander, 2003). This could explain our phase speeds which are lower than in the above mentioned studies.

We find the wave event density in winter to be only 60 % of that in summer. Results from Tang et al. (2014) (data from imager at 40.7° N, 104.9° W) coincide with our results. An explanation for this behaviour could be that the typical altitude for gravity wave breaking is lower in winter than in summer (Holton and Alexander, 2000). This would decrease the number of observed wave events in the airglow layer in winter.

The mean value of horizontal wavelengths in Tang et al. (2014) is roughly 35 km, which is larger than presented here with 20 km (OPN) and 28 km (SBO) and the distribution of periods they determined has a peak around 10 min and a high right-skewness. The peak at the periods we determined is in the same range with 7 to 13 min. The observed phase speed of Tang et al. (2014) has a peak at 50 m s^{-1} and is therefore much higher than in our observations with 22 m s^{-1} (OPN) and 24 m s^{-1} (SBO). Tang et al. (2014) find a major propagation direction to the south in winter which we could determine just for OPN winter. The differences of the stations OPN and SBO could be due to geographical or time-conditioned differences. The former difference could be induced by the underlying orography (the Alps in our measurements), the latter one due to the change of prevailing wind structures. It is interesting to note here that the FOV of SBO is located at the foothills of the Alps (compare Fig. 1). One might suggest here a link to the northward propagating gravity waves in SBO winter which is not present at the other station OPN within the Alpine region.

Intra-diurnal variation can for example be induced by atmospheric tides which change the direction and absolute value of the wind vector within the night and exhibit a period of about 24, 12, and 8 h. However, the 12 h solar tide shows the largest change, at least in the zonal wind (Sandford et al., 2006). Conte et al. (2018) showed that the influence of the 12 h solar tide can be up to 40 m s^{-1} for mid-latitudes (42° N). In order to investigate the possible influence of such phenomena, the relationship between time of day and the direction is determined (see Fig. 5). We find an anti-correlation between the opposing directions (NE and SW, NW and SE). This could be an indication for a tide filtering out waves propagating in one direction and therefore preferring the opposing direction. From theory and observations (e.g. Oberheide et al., 2003; Silber et al., 2017), we know that the diurnal

and semi-diurnal tide are supposed to have the strongest amplitudes, however, also the terdiurnal tide is prominent. Our data show systematic oscillatory patterns of the same order of magnitude, so that we suggest mesospheric tides to be of major influence on the intra-diurnal variability of gravity waves. A more detailed analysis with highly resolved wind data for the Alpine region is needed to verify the presence of tides in the data, but it is beyond the scope of this study.

6 Summary

We have shown two airglow observation data sets with high spatio-temporal resolution. The instrument FAIM was located in the Alpine region first at Oberpfaffenhofen, Germany (OPN, 48.09° N, 11.28° E) and then at Sonnblick Observatory, Austria (SBO, 47.05° N, 12.96° E). The preprocessing as well as the analysis technique based on the two-dimensional fast Fourier transform with automatic peak extraction and grouping into wave events are explained extensively. Combining the phase information of consecutive images allows the derivation of additional parameters related to time, especially horizontal phase speed and wave period. In general, observing the OH airglow layer with our imager allows us to characterise the spectrum of high-frequency gravity waves. The horizontal propagation directions of gravity waves show a clear seasonal dependency to the NE in summer. In winter, they are to the SW at OPN and to the SW or NW at SBO. The zonal directions can be well explained by stratospheric wind filtering while the meridional propagation towards the summer pole (OPN and SBO summer) is not yet completely understood. We suggest the meridional circulation itself to be the reason for the meridional preferential direction which is faster in summer when we observe a stronger filtering than in winter. We assume the generally lower height of gravity wave breaking in winter to be the reason that the gravity wave event density in winter is just 60 % of that in summer. Concerning the observed horizontal phase speeds we find 7 %–9 % higher phase speeds in summer than in winter. The mean phase speeds are 22 m s^{-1} at OPN and 24 m s^{-1} at SBO. Very few events with absolute phase speeds higher than 50 m s^{-1} were found. The intra-diurnal variability is investigated by grouping the gravity waves according to their occurrence time within the night. We find an anti-correlation between opposing directions (NE and SW, NW and SE) and see oscillatory patterns. We assume the reason for it to be the influence of mesospheric tides on gravity wave generation and propagation.

References

Baker, D. J. and Romick, G. J.: The rayleigh: interpretation of the unit in terms of column emission rate or apparent radiance expressed in SI units, Appl. Optics, 15, 1966–1968, 1976.

Baker, D. J. and Stair Jr., A. T.: Rocket Measurements of the Altitude Distributions of the Hydroxyl Airglow, Phys. Scripta, 37, 611–622, 1988.

Becker, E.: Sensitivity of the Upper Mesosphere to the Lorenz Energy Cycle of the Troposphere, J. Atmos. Sci., 66, 647–666, https://doi.org/10.1175/2008JAS2735.1, 2009.

Bradski, G.: The OpenCV Library, Dr. Dobb's Journal of Software Tools, 2000.

Coble, M. R., Papen, G. C., and Gardner, C. S.: Computing Two-Dimensional Unambiguous Horizontal Wavenumber Spectra from OH Airglow Images, IEEE T. Geosci. Remote, 36, 368–382, 1998.

Conte, J. F., Chau, J. L., Laskar, F. I., Stober, G., Schmidt, H., and Brown, P.: Semidiurnal solar tide differences between fall and spring transition times in the Northern Hemisphere, Ann. Geophys., 36, 999–1008, https://doi.org/10.5194/angeo-36-999-2018, 2018.

Dowle, M. and Srinivasan, A.: data.table: Extension of "data.frame", r package version 1.11.8, available at: https://CRAN.R-project.org/package=data.table (last access: 10 January 2019), 2018.

Fleming, E. L., Chandra, S., Barnett, J., and Corney, M.: Zonal mean temperature, pressure, zonal wind and geopotential height as functions of latitude, Adv. Space Res., 10, 11–59, https://doi.org/10.1016/0273-1177(90)90386-e, 1990.

Fritts, D. C. and Alexander, M. J.: Gravity wave dynamics and effects in the middle atmosphere, Rev. Geophys., 41, 1003, https://doi.org/10.1029/2001RG000106, 2003.

Fritts, D. C. and Vincent, R. A.: Mesospheric Momentum Flux Studies at Adelaide, Australia: Observations and a Gravity Wave–Tidal Interaction Model, J. Atmos. Sci., 44, 605–619, https://doi.org/10.1175/15200469(1987)044<0605: MMFSAA>2.0.CO;2, 1987.

Garcia, F. J., Taylor, M. J., and Kelley, M. C.: Two-dimensional spectral analysis of mesospheric airglow image data, Appl. Optics, 36, 7374–7385, 1997.

Garcia, R. R. and Solomon, S.: The effect of breaking gravity waves on the dynamics and chemical composition of the mesosphere and lower thermosphere, J. Geophys. Res., 90, 3850, https://doi.org/10.1029/JD090iD02p03850, 1985.

Gardner, C. S. and Taylor, M. J.: Observational limits for lidar, radar and airglow imager measurements of gravity wave parameters, J. Geophys. Res., 103, 6427–6437, 1998.

Gardner, C. S., Coble, M., Papen, G. C., and Swenson, G. R.: Observations of the unambiguous 2-dimensional horizontal wave number spectrum of OH intensity perturbations, Geophys. Res. Lett., 23, 3739–3742, https://doi.org/10.1029/96gl03158, 1996.

Hannawald, P., Schmidt, C., Wüst, S., and Bittner, M.: A fast SWIR imager for observations of transient features in OH airglow, Atmos. Meas. Tech., 9, 1461–1472, https://doi.org/10.5194/amt-9-1461-2016, 2016.

Hecht, J. H., Fricke-Begemann, C., Walterscheid, R. L., and Höffner, J.: Observations of the breakdown of an atmoshpreic gravity wave near the cold summer mesopause at 54N, Geophys. Res. Lett., 6, 879–882, 2000.

Holton, J. and Alexander, M.: The role of waves in the transport circulation of the middle atmosphere, in: Atmospheric Science Across the Stratopause, Geophysical Monograph, American Geophysical Union, https://doi.org/10.1029/GM123p0021, 2000.

Holton, J. R.: The Influence of Gravity Wave Breaking on the General Circulation of the Middle Atmosphere, J. Atmos. Sci., 40, 2497–2507, https://doi.org/10.1175/1520-0469(1983)040<2497:TIOGWB>2.0.CO;2, 1983.

Kaehler, A. and Bradski, G.: Learning OpenCV3 – Computer Vision in C++ with the OpenCV Library, O'Reilly Media, Sebastopol, USA, 2017.

Kaiser, J. and Schafer, R.: On the Use of the I0-Sinh Window for Spectrum Analysis, IEEE T. Acoust. Speech, 28, 105–107, https://doi.org/10.1109/TASSP.1980.1163349, 1980.

Matsuda, T. S., Nakamura, T., Ejiri, M. K., Tsutsumi, M., and Shiokawa, K.: New statistical analysis of the horizontal phase velocity distribution of gravity waves observed by airglow imaging, J. Geophys. Res.-Atmos., 119, 9707–9718, https://doi.org/10.1002/2014jd021543, 2014.

McLandress, C.: On the importance of gravity waves in the middle atmosphere and their parameterization in general circulation models, J. Atmos. Sol.-Terr. Phy., 60, 1357–1383, https://doi.org/10.1016/S1364-6826(98)00061-3, 1998.

Meinel, A. B.: OH Emission band in the spectrum of the night sky I, American Astronomical Society, 111, p. 555, https://doi.org/10.1086/145296, 1950.

Mukherjee, G. K., R, P. S., Parihar, N., Ghodpage, R., and Patil, P. T.: Studies of the wind filtering effect of gravity waves observed at Allahabad (25.45° N, 81.85° E) in India, Earth Planets Space, 62, 309–318, https://doi.org/10.5047/eps.2009.11.008, 2010.

Nakamura, T., Higashikawa, A., Tsuda, T., and Matsushita, Y.: Seasonal variations of gravity wave structures in OH airglow with a CCD imager at Shigaraki, Earth Planets Space, 51, 897–906, https://doi.org/10.1186/BF03353248, 1999.

Oberheide, J., Hagan, M. E., and Roble, R. G.: Tidal signatures and aliasing in temperature data from slowly precessing satellites, J. Geophys. Res., 108, 1055, https://doi.org/10.1029/2002JA009585, 2003.

Pautet, D. and Moreels, G.: Ground-based satellite-type images of the upper-atmosphere emissive layer, Appl. Optics, 41, 823–831, 2002.

Pautet, P.-D., Taylor, M. J., W. R. Pendleton, J., Zhao, Y., Yuan, T., Esplin, R., and McLain, D.: Advanced mesospheric temperature mapper for high-latitude airglow studies, Appl. Optics, 53, 5934–5943, https://doi.org/10.1364/AO.53.005934, 2014.

Peterson, A. W.: Airglow events visible to the naked eye, Appl. Optics, 18, 3390–3393, https://doi.org/10.1364/ao.18.003390, 1979.

Press, W. H., Teukolsky, S. A., Vetterling, W. T., and Flannery, B. P.: Numerical Recipes, 3rd edn.: The Art of Scientific Computing, Cambridge University Press, New York, NY, USA, 2007.

R Core Team: R: A Language and Environment for Statistical Computing, R Foundation for Statistical Computing, Vienna, Austria, available at: https://www.r-project.org/ (last access: 10 January 2019), 2017.

Rousselot, P., Lidman, C., Cuby, J.-G., Moreels, G., and Monnet, G.: Night-sky spectral atlas of OH emission lines in the near-infrared, Astron. Astrophys., 354, 1134–1150, 2000.

Sandford, D. J., Muller, H. G., and Mitchell, N. J.: Observations of lunar tides in the mesosphere and lower thermosphere at Arctic and middle latitudes, Atmos. Chem. Phys., 6, 4117–4127, https://doi.org/10.5194/acp-6-4117-2006, 2006.

Sedlak, R., Hannawald, P., Schmidt, C., Wüst, S., and Bittner, M.: High-resolution observations of small-scale gravity waves and turbulence features in the OH airglow layer, Atmos. Meas. Tech., 9, 5955–5963, https://doi.org/10.5194/amt-9-5955-2016, 2016.

Silber, I., Price, C., Schmidt, C., Wüst, S., Bittner, M., and Pecora, E.: First ground-based observations of mesopause temperatures above the Eastern-Mediterranean Part I: Multi-day oscillations and tides, J. Atmos. Sol.-Terr. Phy., 155, 95–103, https://doi.org/10.1016/j.jastp.2016.08.014, 2017.

Tang, Y., Dou, X., Li, T., Nakamura, T., Xue, X., Huang, C., Manson, A., Meek, C., Thorsen, D., and Avery, S.: Gravity wave characteristics in the mesopause region revealed from OH airglow imager observations over Northern Colorado, J. Geophys. Res.-Space, 119, 630–645, https://doi.org/10.1002/2013JA018955, 2014.

Taylor, M. J., Ryan, E. H., Tuan, T. F., and Edwards, R.: Evidence of preferential directions for gravity wave propagation due to wind filtering in the middle atmosphere, J. Geophys. Res., 98, 6047–6057, https://doi.org/10.1029/92JA02604, 1993.

Taylor, M. J., Bishop, M. B., and Taylor, V.: All-sky measurements of short period waves image in the OI(557.7 nm), Na(589.2 nm) and near infrared OH and O_2(0,1) nightglow eemission during the ALOHA-93 campaign, Geophys. Res. Lett., 22, 2833–2836, https://doi.org/10.1029/95GL02946, 1995.

Vargas, F., Swenson, G., and Liu, A.: Evidence of high frequency gravity wave forcing on the meridional residual circulation at the mesopause region, Adv. Space Res., 56, 1844–1853, https://doi.org/10.1016/j.asr.2015.07.040, 2015.

von Savigny, C.: Variability of OH(3-1) emission altitude from 2003 to 2011: Long-term stability and universality of the emission rate-altitude relationship, J. Atmos. Sol.-Terr. Phy., 127, 120–128, https://doi.org/10.1016/j.jastp.2015.02.001, 2015.

Wachter, P., Schmidt, C., Wüst, S., and Bittner, M.: Spatial gravity wave characteristics obtained from multiple OH(3-1) airglow temperature time series, J. Atmos. Sol.-Terr. Phy., 135, 192–201, https://doi.org/10.1016/j.jastp.2015.11.008, 2015.

Walterscheid, R., Hecht, J., Vincent, R., Reid, I., Woithe, J., and Hickey, M.: Analysis and interpretation of airglow and radar observations of quasi-monochromatic gravity waves in the upper mesosphere and lower thermosphere over Adelaide, Australia (35° S, 138° E), J. Atmos. Sol.-Terr. Phy., 61, 461–478, https://doi.org/10.1016/s1364-6826(99)00002-4, 1999.

Wickham, H.: ggplot2: Elegant Graphics for Data Analysis, Springer-Verlag New York, available at: https://ggplot2.tidyverse.org/ (last access: 10 January 2019), 2016.

Wüst, S., Wendt, V., Schmidt, C., Lichtenstern, S., Bittner, M., Yee, J.-H., Mlynczak, M. G., and Russell III, J. M.: Derivation of gravity wave potential energy density from NDMC measurements, J. Atmos. Sol.-Terr. Phy., 138–139, 32–46, https://doi.org/10.1016/j.jastp.2015.12.003, 2016.

Wüst, S., Bittner, M., Yee, J.-H., Mlynczak, M. G., and Russell III, J. M.: Variability of the Brunt-Väisälä frequency at the OH* layer height, Atmos. Meas. Tech., 10, 4895–4903, https://doi.org/10.5194/amt-10-4895-2017, 2017.

Wüst, S., Offenwanger, T., Schmidt, C., Bittner, M., Jacobi, C., Stober, G., Yee, J.-H., Mlynczak, M. G., and Russell III, J. M.: Derivation of gravity wave intrinsic parameters and vertical wavelength using a single scanning OH(3-1) airglow spectrometer, Atmos. Meas. Tech., 11, 2937–2947, https://doi.org/10.5194/amt-11-2937-2018, 2018.

Yuan, T., She, C.-Y., Krueger, D. A., Sassi, F., Garcia, R., Roble, R. G., Liu, H.-L., and Schmidt, H.: Climatology of mesopause region temperature, zonal wind, and meridional wind over Fort Collins, Colorado (41° N, 105° W), and comparison with model simulations, J. Geophys. Res., 113, D03105, https://doi.org/10.1029/2007JD008697, 2008.

Zhang, S. D., Huang, C. M., Huang, K. M., Yi, F., Zhang, Y. H., Gong, Y., and Gan, Q.: Spatial and seasonal variability of medium- and high-frequency gravity waves in the lower atmosphere revealed by US radiosonde data, Ann. Geophys., 32, 1129–1143, https://doi.org/10.5194/angeo-32-1129-2014, 2014.